Characterization and Performance Analysis of a Chiral-Metamaterial Channel with Giant Optical Activity for Terahertz Communications

Anna Maria Vegni, Valeria Loscrì

Characterization and Performance Analysis of a Chiral-Metamaterial Channel with Giant Optical Activity for Terahertz Communications

Anna Maria Vegni[a,*], Valeria Loscrí[b]

[a]*Department of Engineering, Roma Tre University, Rome, Italy*
[b]*INRIA Lille-Nord Europe, FUN Research Lab, Lille Nord-Europe, France.*

Abstract

Technology in the THz frequency band has progressed rapidly in the last few years. The THz frequency band offers greater communication bandwidth than microwaves frequencies, and is becoming a standard for nanoscale communications. Traditional channel models for lower frequencies do not take into consideration specific properties as the very high molecular absorption or the very high reflection loss. In addition, in a propagation medium exhibiting a Giant Optical Activity, it is also important to derive the characteristics of the channel affected by chirality effects. This phenomenon occurs in particular material known as chiral-metamaterials in the $(4–10)$ THz band.
The main contribution of this paper consist in the analysis of specific parameters of a chiral-metamaterial, such as the relative electrical permittivity, magnetic permeability and chirality coefficients. These parameters are considered for the channel model derivation both in Line-of-Sight and No Line-of-Sight propagation.

The chiral effect affects the channel through the presence of spectral windows, due to peaks of resonance of chiral parameter. Performance analysis of the chirality-affected channel is assessed in terms of (*i*) channel capacity, (*ii*) propaga-

---

*Corresponding author
Email addresses: annamaria.vegni@uniroma3.it (Anna Maria Vegni), valeria.loscri@inria.fr (Valeria Loscrí)

tion delay, (*iii*) coherence bandwidth, and (*iv*) symbol rates, for different distances and propagation modes.

Keywords: THz band, chirality effects, Giant Optical Activity, nano-communications

1. Introduction

Over the last few years we have witnessed an increasing demand for much higher speed and ubiquitous wireless communication systems. Technological development pave the advent of new communication paradigms, such as the Internet of NanoThings [1]. Following this trend, the THz frequency band is rising as a very promising solution to enable ultra-high-speed communications with the aim to overcome the spectrum scarcity and capacity limitations of current wireless systems. Advanced physical layer solutions are required, able to capture the specific and inherent features of the THz frequency bands. Indeed, traditional channel models for lower frequency bands cannot be adopted for THz communication.

Some new channel models have been presented for THz frequency bands [2, 3, 4, 5, 6], where some of the specific characteristics of this frequency band, such as the high molecular absorption and the spreading loss, are taken into consideration and analyzed. Also, the analysis of signal propagation has been addressed in [7] through a multi-ray approach by assuming reflected, scattered and diffracted paths. As a result, the authors derived the main THz-band channel features, such as the distance-varying spectral windows, and the temporal broadening effects.

As it can be noticed from previous works, channel modeling in THz band is typically addressed through the study of its transfer functions that consider specific features, like molecular absorption loss or spreading loss, among others. However, the previous models take into consideration some specific features of the channel at THz frequencies, but neglect other important effects that could play a very important role in the channel modeling. One of these properties is the electro-magnetic chirality effect and the specific features of the propagation medium. Chirality effect is the characteristic of some natural materials to render an electric/magnetic response (displacement) under a magnetic/electric excitation (field), respectively. This effect can be recognized in the so-called natural/artificial chiral materials. Examples of natural chiral materials are the sugar molecules (sucrose) or the cholesteric liquid crystals. Artificial chiral materials, *e.g.*, sculptured thin films [8], can be obtained by doping a natural dielectric with an amount of metallic/dielectric impurities each working as a couple of interacting electro-magnetic dipoles. These impurities generate the handedness experimental evidence that prevents the superimposition of the molecular structure over a reverse copy of itself.

The relative chirality parameter is an intrinsic characteristic of a chiral homogeneous isotropic medium. Standard values are in the range $[0, 1]$. We observe that in a specific range of the THz band, *i.e.*, $(4$-$10)$ THz, the chiral parameter can reach very high values that vary with the frequency, and show a resonant behavior. Materials with this specific feature are said to exhibit a Giant Optical Activity (GOA). In particular media such as the chiral complex materials where a GOA takes place, the relative chirality parameter is complex and frequency-dependent, showing multiple peaks at specific resonance frequencies [9].

GOA material affected by chirality effects is generally called as *chiral-metamaterial* [10], due to the effect that the real part of relative electric permittivity and magnetic permeability of the material shows negative values, and are frequency-dependent.

This interesting property is of great interest to many areas of science, like analytical chemistry and molecular biology. Finally, chiral-metamaterials are suitable media for the realization of nanosystem applications. Specifically, they represent the ideal candidates for operations in the THz band. In fact, in comparison to natural materials, chiral-metamaterials show a strong response to the THz radiation that represents a great technological potential in several sectors such as imaging, sensing, and also communications.

In this paper, we focus on GOA chiral-metamaterials, derive the channel transfer function and analyze its specific behavior in case of direct and multi-path propagation, in the $(4\text{–}10)$ THz frequency range [9]. Due to the resonant behavior of chiral parameter, the channel model shows specific frequency-dependent spectral windows, guaranteeing high bandwidth values.

This paper is organized as follows. In Section 2 we introduce the frequency-dependent behavior of specific parameters of a chiral-metamaterial. Starting from the concept of electro-magnetic chirality [11, 12, 13], we consider the chiral effects following the change in the propagation velocity and in the refractive index, due to the chiral impurities inside the propagation medium. These effects are evaluated also in the case when the considered medium exhibits a GOA [9, 14]. Then, in Section 3 we derive the corresponding chirality-affected channel model for THz band, and present the related frequency-dependent spectral windows. Section 4 is then devoted to the performances of the chiral channel, assessed in terms of capacity, propagation delay, coherence bandwidth, and symbol rates, in case of LoS and NLoS propagation modes. Finally, conclusions are drawn at the end of the paper.

2. Full-Wave Propagation Model in a Chiral-Metamaterial

Starting from the classic harmonic macroscopic Maxwell's equations, we consider the electro-magnetic propagation inside a generic complex material, under the assumption that it is a linear and chiral medium.

Unconventional materials (*i.e.*, metamaterials) are specifically considered since the GOA is reinforced by using thin metallic crossed-structure impurities in the host dielectric medium, that is chiral-metamaterials [10]. Therefore, we consider a time-harmonic generic linear material, where chiral (magneto/electric-optical) effects are included in the following constitutive relations, written as:

$$\begin{cases} \mathbf{B} = \underline{\xi} \bullet \mathbf{E} + \underline{\mu} \bullet \mathbf{H} \\ \mathbf{D} = \underline{\varepsilon} \bullet \mathbf{E} + \underline{\zeta} \bullet \mathbf{H} \end{cases} \tag{1}$$

where we remind that $\mathbf{B}$ is the magnetic displacement and $\mathbf{H}$ is the magnetic field, as well as $\mathbf{D}$ is the electric displacement and $\mathbf{E}$ is the electric field. Finally, the symbol $\bullet$ represents the scalar product operator, and $\underline{\xi}$, $\underline{\mu}$, $\underline{\varepsilon}$, and $\underline{\zeta}$ are specific tensor quantities of the material.

From (1) we observe the chirality property through the dependence of (*i*) $\mathbf{E}$ in $\mathbf{B}$, and (*ii*) $\mathbf{H}$ in $\mathbf{D}$. Furthermore, the displacement field existing inside the material is generated by an excitation expressed in terms of intensity of the incident electro-magnetic field. Therefore, the material under consideration is a linear chiral medium.

We remind that the chiral effects have a two-fold meaning, *i.e.*, (*i*) an electric field applied on the material provides not only an electric induction, but also a magnetic displacement, and (*ii*) a magnetic field applied on the material provides not only a magnetic induction, but also an electric displacement, unlike from nonchiral materials.

As previously said, in this paper our attention is devoted to GOA chiral-metamaterials [15], where the authors show that for a GOA reciprocal material the specific constitutive relations are as follows:

$$\begin{bmatrix} \mathbf{B} \\ \mathbf{D} \end{bmatrix} = \begin{bmatrix} -j\frac{\xi_0\xi_r}{c} & \mu_0\mu_r \\ \varepsilon_0\varepsilon_r & j\frac{\xi_0\xi_r}{c} \end{bmatrix} \bullet \begin{bmatrix} \mathbf{E} \\ \mathbf{H} \end{bmatrix}, \tag{2}$$

where it is clear that the natural dielectric (where ε_b and μ_b are the permittivity and permeability, respectively) becomes a metamaterial. Moreover, according to [15], at the frequency around 5 THz and 8 THz, there are four resonance frequencies of the ξ_r relative chirality parameter, *i.e.*, $[4.8, 5.6, 7.9, 8.2]$ THz.

The same consideration is applied to the relative permittivity and permeability parameters, still in the (4–10) THz band. As reported in [9, 16], ε_r and μ_r are complex parameters, and the real part has a frequency-dependent behavior with resonant peaks.

Equation (2) becomes

$$\begin{aligned} \begin{bmatrix} \mathbf{B} \\ \mathbf{D} \end{bmatrix} &= \\ &= \begin{bmatrix} -j\frac{\Omega_\xi\omega_0\omega}{\omega_0^2-\omega^2-j\omega\gamma} & \mu_0\left(\mu_b + \frac{\Omega_\mu\omega^2}{\omega_0^2-\omega^2-j\omega\gamma}\right) \\ \varepsilon_0\left(\varepsilon_b + \frac{\Omega_\varepsilon\omega_0^2}{\omega_0^2-\omega^2-j\omega\gamma}\right) & j\frac{\Omega_\xi\omega_0\omega}{\omega_0^2-\omega^2-j\omega\gamma} \end{bmatrix} \bullet \begin{bmatrix} \mathbf{E} \\ \mathbf{H} \end{bmatrix}, \end{aligned} \tag{3}$$

where $\omega = 2\pi f$, ε_0, and μ_0 are the absolute permittivity and permeability, respectively. Then, the constitutive parameters of interest are:

$$\varepsilon = \varepsilon_0 \varepsilon_r = \varepsilon_0 \left[\varepsilon_b + \Omega_\varepsilon \omega_0^2 \left(\frac{\omega_0^2 - \omega^2 + j\omega\gamma}{\left(\omega_0^2 - \omega^2\right)^2 + \omega^2\gamma^2} \right) \right], \tag{4}$$

$$\mu = \mu_0 \mu_r = \mu_0 \left[\mu_b + \Omega_\mu \omega^2 \left(\frac{\omega_0^2 - \omega^2 + j\omega\gamma}{\left(\omega_0^2 - \omega^2\right)^2 + \omega^2\gamma^2} \right) \right], \tag{5}$$

$$\xi_r = \Omega_\xi \omega_0 \omega \left(\frac{\omega_0^2 - \omega^2 + j\omega\gamma}{\left(\omega_0^2 - \omega^2\right)^2 + \omega^2\gamma^2} \right). \tag{6}$$

It is noted that the frequency resonant behavior of ξ_r is a Drude-like one, and Ω_ε, Ω_μ, Ω_ξ, γ, and ω_0 are specific parameters of the GOA material [15].

By simple computations, and assuming a lossy material, *i.e.*,

$$\begin{cases} \varepsilon_b = \mathrm{Re}\left[\varepsilon_b\right] + j\mathrm{Im}\left[\varepsilon_b\right] \\ \mu_b = \mathrm{Re}\left[\mu_b\right] + j\mathrm{Im}\left[\mu_b\right] \end{cases} \tag{7}$$

we obtain

$$\begin{aligned} \varepsilon_r &= \left(\mathrm{Re}\left[\varepsilon_b\right] + \frac{\omega_0^2\left(\omega_0^2-\omega^2\right)\Omega_\varepsilon}{\left(\omega_0^2-\omega^2\right)^2+\omega^2\gamma^2} \right) + \\ & j\left(\frac{\gamma\omega_0^2\Omega_\varepsilon\omega}{\left(\omega_0^2-\omega^2\right)^2+\omega^2\gamma^2} + \mathrm{Im}\left[\varepsilon_b\right] \right), \end{aligned} \tag{8}$$

$$\begin{aligned} \mu_r &= \left(\mathrm{Re}\left[\mu_b\right] + \frac{\omega^2\left(\omega_0^2-\omega^2\right)\Omega_\mu}{\left(\omega_0^2-\omega^2\right)^2+\omega^2\gamma^2} \right) + \\ & j\left(\frac{\gamma\Omega_\mu\omega^3}{\left(\omega_0^2-\omega^2\right)^2+\omega^2\gamma^2} + \mathrm{Im}\left[\mu_b\right] \right), \end{aligned} \tag{9}$$

$$\xi_r = \omega_0 \Omega_\xi \left[\frac{\omega\left(\omega_0^2 - \omega^2\right)}{\left(\omega_0^2 - \omega^2\right)^2 + \omega^2\gamma^2} \right] + j\omega_0\Omega_\xi \left[\frac{\gamma\omega^2}{\left(\omega_0^2 - \omega^2\right)^2 + \omega^2\gamma^2} \right]. \tag{10}$$

Now, by posing the following expression for the square relative refractive index:

$$\begin{aligned}\varepsilon_r\mu_r + \xi_r^2 = & \left(\mathrm{Re}\left[\varepsilon_r\right] + j\mathrm{Im}\left[\varepsilon_r\right]\right)\left(\mathrm{Re}\left[\mu_r\right] + j\mathrm{Im}\left[\mu_r\right]\right) + \\ & + \left(\mathrm{Re}\left[\xi_r\right] + j\mathrm{Im}\left[\xi_r\right]\right)^2 > 0,\end{aligned} \tag{11}$$

we observe that the following conditions hold for a GOA material:

$$\Omega_\varepsilon = \left(1 + \frac{\gamma^2}{\omega^2 - \omega_0^2}\right)\mathrm{Re}\left[\varepsilon_b\right], \tag{12}$$

$$\Omega_\mu = \left(1 + \frac{\gamma^2}{\omega^2 - \omega_0^2}\right)\mathrm{Re}\left[\mu_b\right], \tag{13}$$

$$\Omega_\xi = \left(1 + \frac{\gamma^2}{\omega^2 - \omega_0^2}\right)\sqrt{\mathrm{Re}\left[\varepsilon_b\right]\mathrm{Re}\left[\mu_b\right]}. \tag{14}$$

It is observed that relations (12), (13), and (14) state the connection between the host material parameters, *i.e.*, ε_b, and μ_b, and the specific GOA ones in order to obtain a positive refractive index in (11).

Finally, the computation of the electro-magnetic field in the channel is carried out through the solutions of linear differential equations, arising from the following source-less Maxwell's equations:

$$\begin{cases} \left(\underline{\nabla} + j\omega\underline{\xi}\right) \bullet \mathbf{E} = -j\omega\underline{\mu} \bullet \mathbf{H} \\ \left(\underline{\nabla} - j\omega\underline{\zeta}\right) \bullet \mathbf{H} = j\omega\underline{\varepsilon} \bullet \mathbf{E} \end{cases} \tag{15}$$

and the solving differential equations for $\mathbf{E}$ and $\mathbf{H}$ are given, respectively:

$$\begin{cases} \left[\left(\underline{\nabla} - j\omega\underline{\zeta}\right) \bullet \underline{\mu}^{-1} \bullet \left(\underline{\nabla} + j\omega\underline{\xi}\right) - \omega^2\underline{\varepsilon}\right] \bullet \mathbf{E} = 0 \\ \left[\left(\underline{\nabla} + j\omega\underline{\xi}\right) \bullet \underline{\varepsilon}^{-1} \bullet \left(\underline{\nabla} - j\omega\underline{\zeta}\right) - \omega^2\underline{\mu}\right] \bullet \mathbf{H} = 0 \end{cases} \tag{16}$$

where $\underline{\nabla}$ is Kong's operator.

As a noteworthy point, we can examine how the constitutive relations influence the channel polarization properties. Typically, the antenna at the transmitter side is a radiating element that can be linearly or circularly polarized. In these two cases we obtain interesting features of the channel directly connected with the constitutive relations of the medium. Namely, by assuming the linear polarization of the electric field generated by an appropriate antenna (*i.e.*, $\mathbf{E} = E_x\hat{\mathbf{x}}$), we obtain the final second order partial differential equation for E_x, *i.e.*,

$$\alpha_1 E_x + \alpha_2 \frac{\partial E_x}{\partial x} + \alpha_3 \frac{\partial E_x}{\partial y} + \alpha_4 \frac{\partial E_x}{\partial z} + \alpha_5 \frac{\partial^2 E_x}{\partial y^2} + \alpha_6 \frac{\partial^2 E_x}{\partial z^2} = 0, \tag{17}$$

where α_i with $i = (1, 2, \ldots, 6)$ are coefficients depending on the elements of $\underline{\varepsilon}$, $\underline{\mu}$, $\underline{\xi}$, and $\underline{\zeta}$ tensors.

On the other side, for a circularly polarized antenna, *i.e.*, $\mathbf{E} = E_x\hat{\mathbf{x}} + E_y\hat{\mathbf{y}} = E_x\hat{\mathbf{x}} + j\,(\pm)\,E_x\hat{\mathbf{y}}$, the final second order partial differential equation for E_x is obtained:

$$\gamma_1 E_x + \gamma_2 \frac{\partial^2 E_x}{\partial x^2} + \gamma_3 \frac{\partial^2 E_x}{\partial x \partial y} + \gamma_4 \frac{\partial^2 E_x}{\partial x \partial z} + \gamma_5 \frac{\partial^2 E_x}{\partial y^2} + \gamma_6 \frac{\partial^2 E_x}{\partial y \partial z} + \gamma_7 \frac{\partial^2 E_x}{\partial z^2} = 0, \tag{18}$$

where γ_j with $j = (1, 2, \ldots, 7)$ are coefficients depending on the elements of $\underline{\varepsilon}$, $\underline{\mu}$, $\underline{\xi}$, and $\underline{\zeta}$ tensors. Equations (17) and (18) allow to classify the transmission properties of the channel according to the choice of the transmitting medium. Therefore, such formulas are useful as design tools for materials working in THz band, including GOA materials and optical metamaterials.

Notice that α_i and γ_j parameters can be described through 36 degrees of freedom as a consequence of their dependance on $\underline{\varepsilon}$, $\underline{\mu}$, $\underline{\xi}$, and $\underline{\zeta}$ tensors. This means that we have a lot of partial differential linear equations similar to (17) and (18) that should be examined in order to determine the corresponding propagation characteristics of the channel. However, as future work, we can investigate this point by starting from a topology of channel material (*e.g.*, bianisotropic, biaxial, etc.) and then determine the specific transmission/ reflection related properties.

3. Chiral-affected Channel Model

In this section, we present how the relative chiralilty parameter affects the channel performance in the $(4–10)$ THz band, in the case of ray tracing propagation (*i.e.*, LoS, and NLoS), and under the linear polarization hypothesis. Specifically, in NLoS case, we focus on reflected paths due at generic reflection centers located at z-plane. The reflection characteristics of the transmissive channel can be evaluated through the specific knowledge of the local planar geometry associated to the reflection centers.

The use of ray tracing techniques for channel modeling in THz band has been largely adopted, like in [5], where Han *et al.* consider a multi-ray approach with one direct path, and other reflected, scattered, and diffracted paths. According to this approach, the channel model is the combination of several individual narrow sub-bands, each of them with a flat-band response. Assuming N_i narrow sub-bands, and in the case of stationary environment, the channel response in the i-th sub-band is given as

$$h_i\left(\tau\right) = \sum_{n=1}^{N_i} \alpha_{i,n} \delta\left(\tau - \tau_n\right), \tag{19}$$

where $\alpha_{i,n}$ is the frequency-dependent attenuation, and τ_n is the propagation delay of the n-th ray in the multi-ray approach.

From (19), and according to the computations in [5], we can derive the LoS and NLoS channel transfer functions in the case of chirality-affected channel with GOA, respectively as:

$$H_{\mathrm{LoS}}\left(f\right) = H_{\mathrm{Abs}}\left(f\right) H_{\mathrm{Spr}}\left(f\right) e^{-j2\pi f \tau_{\mathrm{LoS}}}, \tag{20}$$

and

$$H_{\mathrm{NLoS}}\left(f\right) = \left[\frac{\nu_c}{4\pi f\left(d_1+d_2\right)}\right] e^{-j2\pi f \tau_{\mathrm{NLoS}} - \frac{1}{2}k(f)(d_1+d_2)} \cdot R\left(f\right), \tag{21}$$

where we assume the NLoS scenario is affected by reflected rays only, through the rough surface reflection loss, *i.e.*, $R(f)$.

In (20), H_{Abs} is the transfer function due to the molecular absorption loss, while H_{Spr} is the spreading loss that takes account for the chirality effect through ν_c that is the propagation velocity of the electro-magnetic field in a chiral homogeneous isotropic medium, *i.e.*,

$$\nu_c = \frac{c}{n_c}, \tag{22}$$

where c is the light propagation speed, and n_c is the refractive index in a chiral medium, *i.e.*,

$$n_c = \sqrt{\mu_r \varepsilon_r + \xi_r^2}, \tag{23}$$

with μ_r, ε_r and ξ_r frequency-dependent parameters, as depicted in [16]. Finally, under the hypothesis of stationary scenario where the transmitter and the receiver are at a distance d [m], from (20) we obtain the propagation delay for the LoS ray as:

$$\tau_{\mathrm{LoS}} = \frac{d}{\nu_c}. \tag{24}$$

For the NLoS channel transfer function expressed in (21), by assuming d_1 as

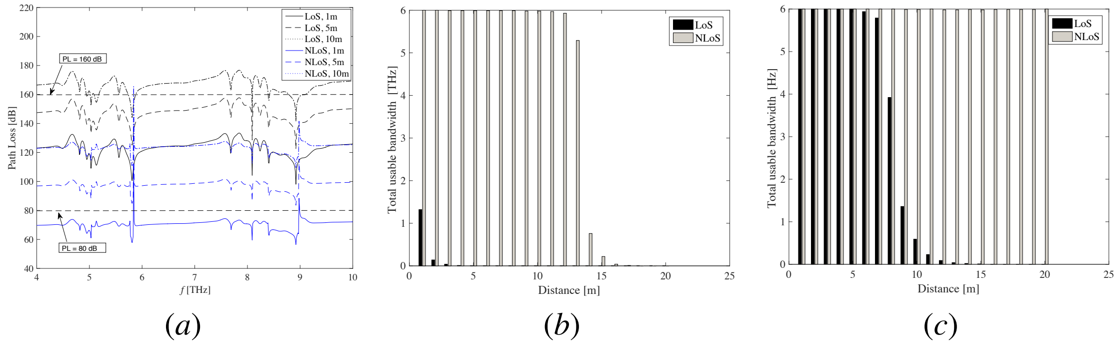

Figure 1: Spectral windows in a chiral-affected channel with GOA. (*a*) Path loss, and (*b*) total usage bandwidth for LoS and NLoS propagation in case of a path loss threshold of 120 dB, and (*c*) 160 dB.

the distance between the transmitter and a generic reflecting point, and d_2 as the distance between this point and the receiver, we obtain the propagation delay of the j-th NLoS ray along the distance $(d_1 + d_2)$, as

$$\tau_{\text{NLoS}} = \frac{d_1 + d_2}{\nu_c}. \tag{25}$$

From the expressions of channel transfer functions in (20) and (21), it is easy to compute the total path loss, as depicted in Figure 1 (*a*) in case of LoS and NLoS propagations, for different distances from transmitter to receiver, and assuming a specific reflecting angle for multi-path. The expressions of path loss in LoS and NLoS are respectively:

$$A_{\text{LoS}} = A_s + A_a = 20\log_{10}\left(\frac{4\pi d}{\lambda_{\text{Chir}}}\right) + 10\gamma d \log_{10} e, \tag{26}$$

and

$$A_{\mathrm{NLoS}} = 10\log_{10}\left(\frac{\nu_c}{4\pi f(d_1+d_2)}\right) + \\ +10\log_{10}\left(e^{-\frac{1}{2}\alpha(d_1+d_2)}e^{-\frac{2\cos(\beta_i)}{\sqrt{n_c^2-1}}}e^{-\frac{8\pi^2 f^2\sigma^2\cos^2(\beta_i)}{\nu_c^2}}\right). \tag{27}$$

where $\lambda_c = \nu_c/f$ is the wavelength in the considered medium affected by the homogeneous chirality, and γ is the absorption coefficient measuring the amount of absorption loss of the EM field in the medium.

From Figure 1, by increasing the distance, the path loss has a higher trend. Moreover, similarly to the results in [7], the LoS propagation (black lines) provides higher values with respect to the NLoS scenario (blue lines). In both LoS and NLoS, the behavior is frequency-dependent, but in LoS propagation the path loss has a smoother trend, with some peaks at 5.8, 8.09 and 8.93 THz. On the other hand, for NLoS propagation, the peaks are well noticeable at 5.8 and 8.93 THz, while on the other frequencies, the trend is on average flat around 70, 100 and 120 dB for LoS at $d = 1$, 5, and 10 m, respectively.

Similarly to the analysis conducted in [7], we aim to characterize the spectral windows of chiral channel transfer functions in case of LoS and NLoS propagation. A spectral window is given by the portion of spectrum below a given path loss threshold. We expect to observe that the path loss peaks caused by the chiral effect create several spectral windows, with different bandwidths in each of them.

In the case of a path loss threshold set to 80 dB, the communication distance is limited for NLoS propagation at lower distance of 1 m, except the two peaks that are above this threshold, and correspond to 5.84 THz and 8.98 THz. According to the values assumed in [7], the threshold of 80 dB corresponds to no gains of transmission and reception antennas, and so to a multi-path propagation model.

In order to identify the spectral windows for LoS propagation, we have to increase the path loss threshold around 120 dB, so that a few windows appear for a distance of 1 m (see curve LoS for $d = 1$ m in Figure 1 (a)). However, in this case most of the path loss for LoS propagation is above the threshold, thus providing a reduced usable bandwidth. Figure 1 (b) depicts the usable bandwidth versus the distance for the path loss threshold of 120 dB. We notice that the available spectrum in LoS propagation is limited up to 4 m, reaching a maximum at 1.32 THz corresponding to a distance of 1 m. In contrast, the NLoS propagation reaches higher bandwidths, and then it decreases at 17 m where the bandwidth is 0.01 THz. The bandwidth rate in LoS is 75.5 GHz/m, while it reaches 3.90 THz/m in NLoS scenario.

It follows that an increase of the path loss threshold to 160 dB is expected to provide higher values of usable bandwidth in LoS propagation, as depicted in Figure 1 (c). Higher path loss thresholds rise from higher antenna gains, and the transmission becomes directional through the LoS path. In this case, the usable bandwidth in LoS propagation reaches higher values than those for the threshold of 120 dB. The lowest value is 0.01 THz for a distance of 15 m, and the average bandwidth rate for LoS propagation is 2.39 THz/m.

On the other side, for NLoS propagation, the usable bandwidth reaches approximately the maximum value of 6 THz for different distances, and then the average rate of the total usable bandwidth is 5.99 THz/m. As a result, we can conclude that within the range (4–10) THz the available bandwidth is almost the entire band, especially for NLoS propagation.

Notice that in this paper, we focus only on the transfer functions in LoS and NLoS scenarios in a chirality-affected channel, assuming a flat behavior for the molecular absorption loss (frequency independent behavior). Then, in all the simulation results we omit the frequency-dependent molecular absorption effect. Specifically, in NLoS we assume the presence of reflected rays only, since we are interested in the behavior of highly frequency-dependent reflections that depend on the shape, material, and roughness of the reflecting surface affects the THz wave propagation.

4. Chiral Channel Characterization

Following the chirality-affected channel model presented in Section 3, in this section we investigate its main features in the $(4–10)$ THz band. Specifically, we aim to characterize (*i*) the channel capacity, (*ii*) the propagation delay, (*iii*) the coherence bandwidth, and (*iv*) the symbol rate.

4.1. Channel capacity and propagation delay

To evaluate the capacity limits in a chiral medium, we refer to the approach adopted in [5], where the received signal has been decomposed as a sum of the sub-bands, each one with a narrow behavior and a flat-band response. The following constraint is adopted:

$$\sum_{i=1}^{N_B} P_i \leq P_{TOT}, \tag{28}$$

where N_B is the total number of sub-bands, P_i is the transmission power in the i-th sub-band, and P_{TOT} is the total transmit power in the $(4–10)$ THz band. Notice that, since the chiral parameter has a frequency-dependent behavior in (4–10) THz band, we consider only this frequency range.

For N_B sub-bands, the capacity can be defined as the sum of the single capac-

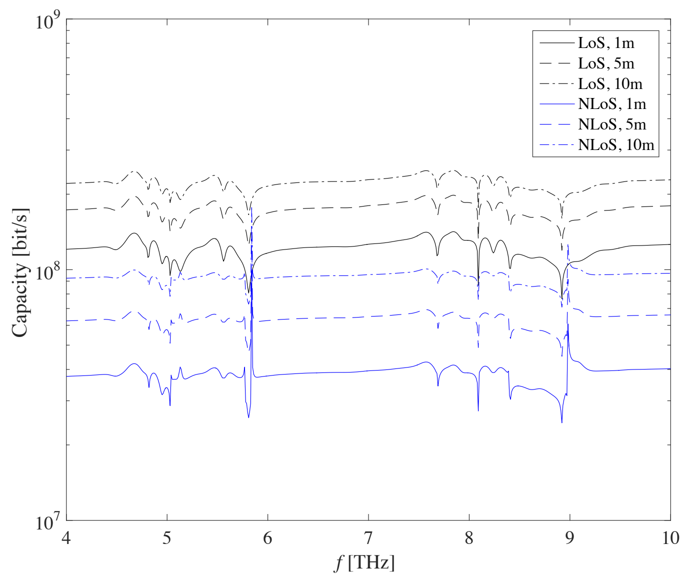

Figure 2: Capacity per sub-band of a chirality-affected channel with GOA, versus frequency for LoS and NLoS propagation, and different distances.

ities in each sub-band, *i.e.*,

$$C = \sum_{i=1}^{N_B} C_i = \sum_{i=1}^{N_B} \Delta f_i \log \left(1 + \frac{|h_i|^2 P_i}{\Delta f_i S_N (f_i)} \right), \tag{29}$$

where S_N is the power spectral density of the additive white Gaussian noise, and Δf_i is the sub-band range among two consecutive sub-bands, *i.e.*, $\Delta f_i = f_{i+1} - f_i$, assumed as 10 GHz in our simulation results. We assume a flat power profile, that is the total power transmission is uniformly distributed over the entire operative band (*i.e.*, from 4 to 10 THz). Also, we consider a power level of 46 dBm, divided across all the sub-bands, *i.e.*, $N_B = 600$.

Figure 2 depicts the chirality-affected channel capacity with GOA in case of LoS and NLoS scenario. We notice that with a reduction of distance, the capacity decreases as well, and also the LoS scenario has a smoother behavior with respect

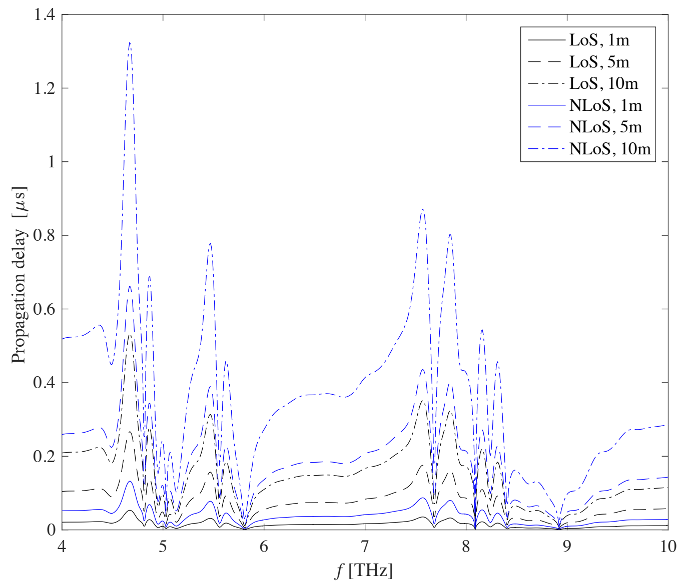

Figure 3: Propagation delay versus frequency in a chirality-affected channel with GOA, for LoS and NLoS propagation, and different distances.

to the frequency, while the NLoS shows an accentuate frequency-dependent trend, with distinguishable peaks at resonance frequencies. Specifically, in LoS, the capacity has an almost flat behavior, with a mean value of 0.22 Gbit/s for $d = 10$ m. Performances get worst in the case of NLoS propagation for $d = 1$ m, where we observe a degradation of capacity at 5.81 and 8.92 THz, corresponding to 25.65 Mbit/s and 24.47 Mbit/s, respectively.

From the expressions in (24) and (25), the propagation delay in LoS and NLoS scenarios is depicted in Figure 3. We observe the frequency-dependent behavior due to the chiral effect, and as expected, performance gets worst when the distance increases. An almost-flat behavior is shown for LoS at short distances (*i.e.*, $d = 1$ m), while a resonant trend appears when increasing the distance, as well as in NLoS scenario due to the longer distances covered. Finally, we observe that the propagation delay both in LoS and NLoS case shows lower values corresponding to 5.81 and 8.92 THz.

4.2. Coherence bandwidth and symbol rate

The root mean square (rms) delay spread is a measure of how dispersive the channel is. It is expressed as [7]:

$$\sigma_i = \sqrt{\overline{\tau_i^2} - \bar{\tau}_i^2}, \tag{30}$$

where $\overline{\tau_i}$ and $\bar{\tau}_i^2$ are the first and second moments of the instantaneous power-delay profile, respectively. From (30) we can derive information about the coherence bandwidth, defined as the range of frequencies over which the channel correlation exceeds 50%.

In our simulations, we consider two scenarios with a variable number of NLoS reflected rays, *i.e.*, (*i*) one, and (*ii*) five, and one direct ray. In both cases, we observe the frequency-dependent behavior as typical of chiral materials exhibiting GOA. In Figure 4 (*a*) we show the coherence bandwidth in the case of one LoS and one NLoS path for different distances. As experienced in [5], higher values are reached for shorter distances. However, we cannot compare our results to others obtained with pre-existing approaches, since the frequency range is not the same.

In our simulations, several peaks appear due to the chirality effects. This can allow tuning the frequency to resonant peaks in order to obtain higher performances. For example, for $d = 1$ m, the minimum value of rms delay is 0.33 ns, corresponding to 8.92 THz. This value corresponds to a symbol rate limited to $0.1/\sigma_i = 0.29$ Gbit/s to avoid inter-symbol interference. Also, in this case, the coherence bandwidth is limited to 0.59 GHz at the frequency peak of 8.92 THz.

On the other side, when the distance increases (*i.e.*, $d = 10$ m), the minimum rms delay is 3.6 ns at 8.92 THz. This value provides a symbol rate limited to 27.71 Mbit/s, and the coherence bandwidth equals to 55.43 MHz, still at the same frequency.

Performances get worst in case of multiple reflected paths, as shown in Figure 4 (b). For $d = 1$ m the minumum rms is 0.78 ns, which corresponds to a coherence bandwidth of 0.25 GHz. For higher distances (*i.e.*, $d = 10$ m) the minimum rms is 7.31 ns, corresponding to a coherence bandwidth is 27.3 MHz.

Finally, following the analysis of coherence bandwidths, we can derive the symbol rates in different scenarios, as depicted in Figure 5 (a) and (b) in case of (a) one LoS and one NLoS path, and (b) one LoS and five reflected NLoS paths, respectively. We notice the symbol rate is limited to a maximum of 0.29 Gbit/s corresponding to 8.92 THz, in order to avoid InterSymbol Interference (ISI) for linearly-modulated signals. Again, the chiral frequency behavior is observed, and a decrease of symbol rate is experienced for increasing distances (*e.g.*, for $d = 10$ m the symbol rate reaches 0.27 Mbit/s at 4.67 THz). Finally, as depicted in Figure 5 (b) an increase of reflected NLoS paths affects the symbol rate, then causing a decrease of performances until 0.13 Mbit/s for $d = 10$ m at 4.67 THz, while the maximum value is 0.12 Gbit/s obtained for $d = 1$ m at the frequency of 8.92 THz.

5. Conclusions

In this paper we have derived the channel transfer function of a GOA chirality affected channel, both in the case of LoS and NLoS propagation in the $(4–10)$ THz band.

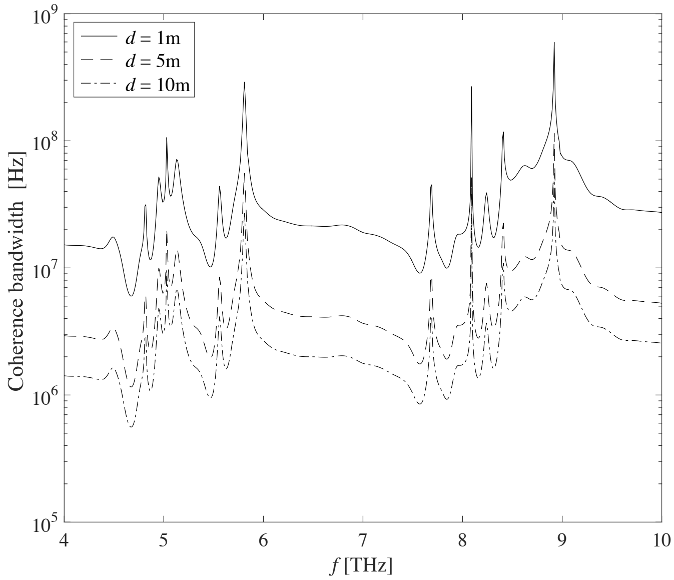

(*a*)

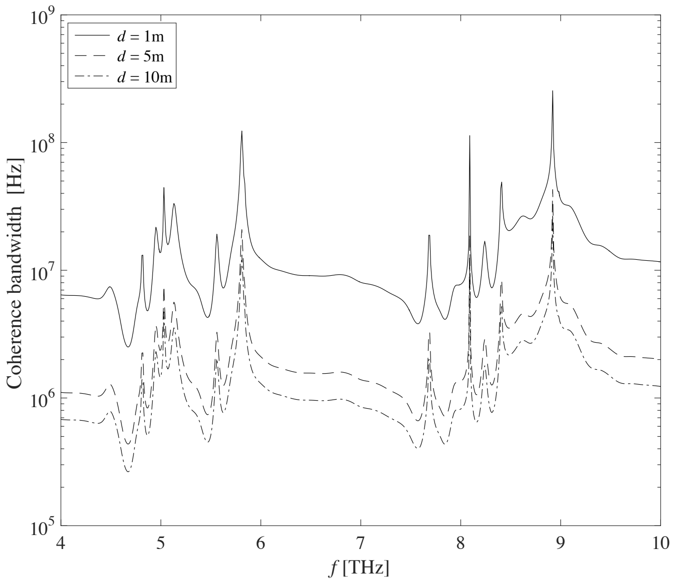

(*b*)

Figure 4: Coherence bandwidth in a chirality-affected channel with GOA, in case of (*a*) one LoS and one NLoS path, an (*b*) one LoS and five NLoS paths.

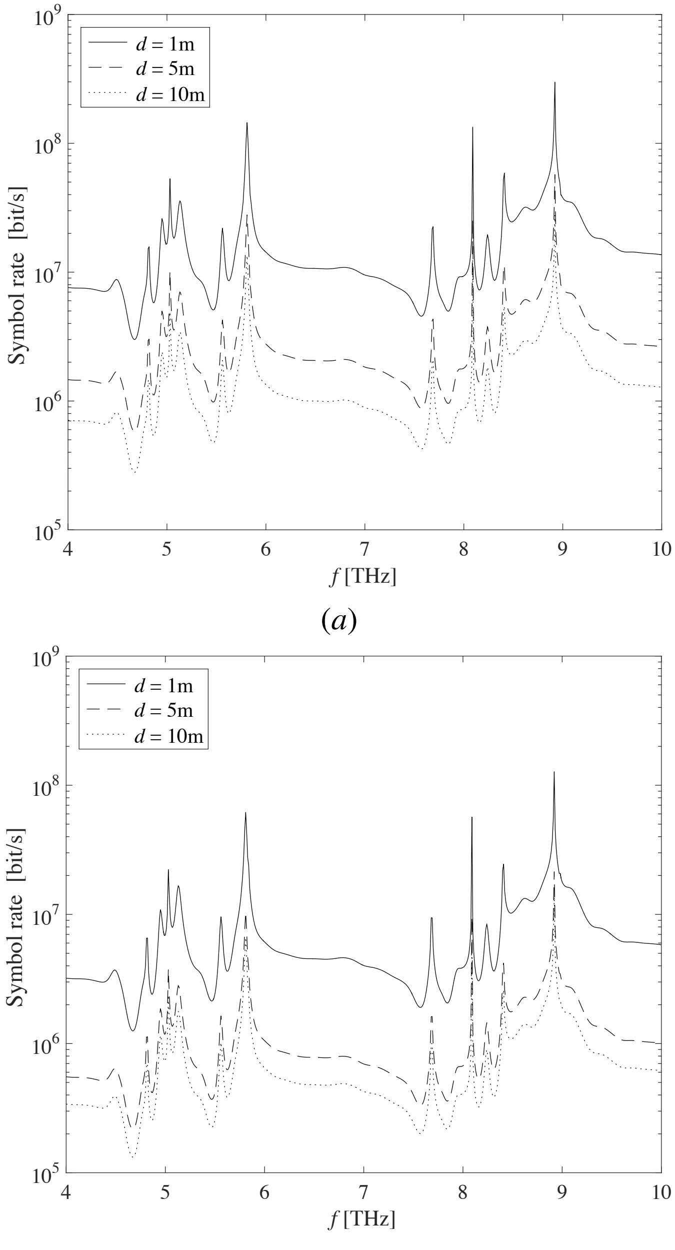

(a)

(b)

Figure 5: Symbol rates versus frequency in a chirality-affected channel with GOA, for different distances from transmitter to receiver, in case of (a) one LoS and one NLoS path, an (b) one LoS and five NLoS paths.

We considered the effects of the relative chiral parameter, assuming a frequency-dependent behavior with resonant peaks at specific frequencies. As a result, this affects the channel transfer function, as well as other performances. In particular, we identified the spectral windows that rise from the chiral effect, and the associated usable bandwidths. The spectral windows vary with the distance and the frequency, with corresponding bandwidths up to 6 THz, both in LoS and NLoS propagation. Another contribution of the paper has been in the identification of specific frequencies that allow high performance to be achieved. Thanks to the frequency-dependent behavior of a chiral-metamaterial, we can tune the working frequency in order to maximize the performance. Just as an example, the rms delay is dependent on the distance and carrier frequency, and reaches minimum values at 8.92 THz, corresponding to higher coherence bandwidths.

As conclusion of this paper, we can claim that GOA metamaterial presenting chirality effects, are really promising in terms of performance that can be achieved, above all in the case of lower distances. Also, distance-adaptive and multi-carrier transmissions represent the more appropriate communication techniques that can benefit from the relationship between distance and bandwidth in the range $(4–10)$ THz.

References

[1] I. F. Akyildiz, J. M. Jornet, The Internet of Nano-Things, IEEE Wireless Communication Magazine 17 (6) (2010) 58–63.

[2] J. Jornet, I. Akyildiz, Channel modeling and capacity analysis for electromagnetic wireless nanonetworks in the terahertz band, Wireless

Communications, IEEE Transactions on 10 (10) (2011) 3211–3221. doi:10.1109/TWC.2011.081011.100545.

[3] I. Llatser, A. Mestres, S. Abadal, E. Alarcon, H. Lee, A. Cabellos-Aparicio, Time- and frequency-domain analysis of molecular absorption in short-range terahertz communications, Antennas and Wireless Propagation Letters, IEEE 14 (2015) 350–353. doi:10.1109/LAWP.2014.2362194.

[4] G. Piro, K. Yang, G. Boggia, N. Chopra, L. Grieco, A. Alomainy, Terahertz communications in human tissues at the nanoscale for healthcare applications, Nanotechnology, IEEE Transactions on 14 (3) (2015) 404–406. doi:10.1109/TNANO.2015.2415557.

[5] C. Han, A. Bicen, I. Akyildiz, Multi-ray channel modeling and wideband characterization for wireless communications in the terahertz band, Wireless Communications, IEEE Transactions on 14 (5) (2015) 2402–2412. doi:10.1109/TWC.2014.2386335.

[6] C. Zhang, C. Han, I. F. Akyildiz, Three dimensional end-to-end modeling and directivity analysis for graphene-based antennas in the terahertz band, in: 2015 IEEE Global Communications Conference (GLOBECOM), 2015, pp. 1–6. doi:10.1109/GLOCOM.2015.7417131.

[7] C. Han, A. Bicen, I. Akyildiz, Multi-wideband waveform design for distance adaptive wireless communications in the terahertz band, Signal Processing, IEEE Transactions on 64 (4) (2016) 910–922.

[8] A. Lakhtakia, R. Messier, Sculptured thin films: nanoengineerred morphology and optics, SPIE Press monograph, 2015.

[9] F. Fang, Y. Cheng, Dual-band terahertz chiral metamaterial with giant optical activity and negative refractive index based on cross-wire structure, Progress In Electromagnetics Research M 31 (2013) 59–69.

[10] B. Wang, T. Koschny, M. Kafesaki, C. M. Soukoulis, Chiral metamaterials: Simulations and experiments, J. Opt. A: Pure Appl. Opt. 11.

[11] N. Engheta, Chiral Materials and Chiral Electrodynamics: Background & Basic Physical Principles, in: Special Workshop on Chiral and Complex Materials Progress in Electromagnetics Research Symposium, 1991.

[12] A. Lakhtakia, Recent contributions to classical electromagnetic theory of chiral media: what next?, Speculations in Science and Technology 14 (1) (1991) 2–17.

[13] I. Lindell, A. Sihvola, S. Tretyakov, A. Viitanen, Electromagnetic waves in chiral and bi-isotropic media, Artech House, 1994.

[14] J. Zhou, D. R. Chowdhury, R. Zhao, A. Azad, H.-T. Chen, C. M. Soukoulis, A. J. Taylor, Terahertz chiral metamaterials with giant and dynamically tunable optical activity, Phys. Rev. B 86. doi:10.1103/PhysRevB.86.035448. URL `http://link.aps.org/doi/10.1103/PhysRevB.86.035448`

[15] R. Zhao, T. Koschny, C. M. Soukoulis, Chiral metamaterials: retrieval of the effective parameters with and without substrate, Optics express 18 (4).

[16] A. M. Vegni, V. Loscrí, Performance of a Chirality-affected Channel exhibiting Giant Optical Activity for Terahertz Communications, in: accepted to ACM NanoCom 2016, 2016, pp. 1–6.